Enhancing the conductivity, stability and flexibility of $Ti_3C_2T_x$ MXenes by regulating etching conditions

Yina Yang[a,b,c], Zherui Cao[a,b], Liangjing Shi[a], Ranran Wang[a,*], Jing Sun[a,*]

[a] *State Key Laboratory of High Performance Ceramics and Superfine Microstructure Shanghai Institute of Ceramics Chinese Academy of Science, Shanghai 200050, China*
[b] *University of Chinese Academy of Sciences, Beijing 100049, China*
[c] *State Key Laboratory of Robotics, Shenyang Institute of Automation, Chinese Academy of Science, 110016, China*

A B S T R A C T

Two-dimensional transition metal carbides or/and nitrides (MXenes) exhibit great development prospects in energy storage, catalysis, sensing and other fields due to their good properties. However, MXenes obtained from different etching conditions show great discrepancy on their electrical and mechanical properties, which will affect their applications to a certain degree. Unfortunately, few reports have systematically investigated such discrepancy and the underlying mechanism. Herein, three etchants and corresponding subsequent operations were used to synthesize three different $Ti_3C_2T_x$ (MXene) samples. The difference in chemical components, morphology and surface terminations of $Ti_3C_2T_x$ and their influences on the conductivity, stability and flexibility were comprehensively analyzed. The underlying mechanism has been investigated simultaneously. Based on this, favorable annealing treatments and storage conditions are also proposed to optimize the properties of $Ti_3C_2T_x$, which is believed of great meaning to the practical applications of $Ti_3C_2T_x$.

1. Introduction

MXenes is a new class of transition metal carbides or/and nitrides that belong to two-dimensional materials, whose chemical formula is $M_nX_{n+1}T_x$ (M represents transition metal, X is carbides or/and nitrides, n = 1, 2, 3, T stands for the surface termination of MXenes, x is the number of T) [1–4]. In 2011, Yury Gogotsi et al selectively etched away the A atomic layer in the three dimensional layered structure of MAX phase (A is main group element) by hydrofluoric acid (HF) and successfully obtained the first kind of MXenes——$Ti_3C_2T_x$, which is the most commonly used MXene material prepared by the mature preparation process [1]. Currently, more than 20 kinds of MXene materials such as T_2CT_x, Ti_3CNT_x, $Ta_4C_3T_x$, etc. [5] have been successively prepared. As two-dimensional materials, MXenes have many characteristics similar to graphene, including metal-like conductivity, large specific surface area, good hydrophilicity and mechanical performance [6–9], making MXenes very promising in the applications in energy storage [10–12], electromagnetic shielding [13–15], catalysis [16–17], sensors and so on [18–20]. During the aqueous etching progress to remove the A atomic layer, the M-A metal bonds are broken, and the exposed M atoms all need to find suitable ligands, and usually combine with the abundant ions present in the reaction environment to form surface terminations, such as −OH, −O and −F [1–2,5]. It is worth

noting that the type and amount of the surface terminations have a great influence on the electronic structure and physicochemical properties of MXenes according to the theoretical calculations [21–23]. For example, the bandgap of $Ti_3C_2(OH)_x$ and $Ti_3C_2F_x$ are 0.05 eV and 0.1 eV respectively, which endow them with many differences in the properties, such as the conductivity and the dispersibility in aqueous solution [1,24–25]. Besides, the different interactions between adjacent primitives caused by different morphologies will also affect the properties of mxenes, such us fiexibility and conductivity that is greatly influenced by contact resistance.

For diverse application, the requirements for the properties of mxenes are different, which means that the requirements for morphology and surface surface terminations are also different. For instance, O terminated MXenes are predicted to exhibit a higher electrocatalytic activity in hydrogen evolution reaction (HER) and a higher capacity in lithium-ion and other batteries than F-terminated MXenes [26], while the later ones are more suitable for nanogenerators due to the large electronegativity of the F atoms [27]. In terms of the requirements of morphology, for example, MXenes with small lateral size are intended to be employed in photothermal therapy and photocatalysis while the large-size flakes are more suitable for constructing three-dimensional (3D) architectures, like aerogel and the products of 3D printing, which are usually applied in electromagnetic shielding,

wearable electronics and so on [11,28–31]. Therefore, regulating the morphologies and surface termination for specific applications is of great importance.

The morphologies and surface terminations of MXenes have a great relationship with the experiment conditions of various preparation methods. Taking $Ti_3C_2T_x$ as an example, since Al in the parent phase MAX has amphoteric properties, both acidic and alkaline reagents can be employed as etchants. HF, tetramethylammonium hydroxide (TMAOH) [32], lithium fluoride (LiF)/hydrochloric acid (HCl) are all commonly used [33]. However, the differences in morphologies and chemical properties of the samples prepared with various etchants have not been systematically studied, and few reports investigated the influence of surface terminations and morphology on the properties of MXenes experimentally to enhance the target properties.

Herein, we respectively applied HF, LiF/HCl, and TMAOH as etchants and controlled the experimental conditions in aqueous etching progress to synthesize three different $Ti_3C_2T_x$ samples and enhance the propertites of $Ti_3C_2T_x$. The difference in chemical components, morphology and surface terminations of $Ti_3C_2T_x$ are analyzed comprehensively. Their influences on the conductivity, stability as well as flexibility were investigated systematically and the underlying mechanism was discovered. Based on this, favorable post treatments and storage conditions have been proposed, which are meaningful to both fundamental research and practical applications of $Ti_3C_2T_x$ MXene.

2. Material and methods

2.1. Materials

Ti_3AlC_2 was purchased from Forsman Scientific (Beijing, Co., Ltd.). Hydrofluoric acid (HF), hydrochloric acid (HCl), Lithium fluoride (LiF) and dimethyl sulfoxide (DMSO) were purchased from China National Medicines Corporation Ltd. Tetramethylammonium hydroxide was purchased from Sigma-Aldrich.

2.2. The fabrication of HF-$Ti_3C_2T_x$

The synthesis of HF-$Ti_3C_2T_x$ was mentioned in the previous work [19]. In detail, the Ti_3AlC_2 powder was mixed with 40 wt% HF with the ratio of 1 g: 10 ml, and was then magnetically stirred for 18 h at room temperature. After that the mixture was washed several times with deionized water until the pH value was over 6, and was dried in a freeze drying oven for 12 h to obtain multilayer $Ti_3C_2T_x$ (m-HF-$Ti_3C_2T_x$).1g m-$Ti_3C_2T_x$ powder was immersed into 12 ml DMSO and the mixture was reacted for 18 h at room temperature. The DMSO was removed by centrifugal washing with deionized water. Then the m-$Ti_3C_2T_x$ paste was dispersed into 300 ml deionized water, which was followed by 2 h of sonication under Ar atmosphere and 1 h of centrifugation at 3500 rpm, the obtained upper suspension was delaminated $Ti_3C_2T_x$ (HF-$Ti_3C_2T_x$).

2.3. The fabrication of TM-$Ti_3C_2T_x$

The synthesis of TM-$Ti_3C_2T_x$ was presented in the previous work. Firstly, 10 ml 20 wt% HF was reacted with 1 g Ti_3AlC_2 for 30 min to remove the oxidation layer of Ti_3AlC_2, then the mixture was washed with deionized water for several times to remove the residual HF and dried. The treated Ti_3AlC_2 powder was stirred magnetically with TMAOH at the ratio of 1 g: 12 ml for 24 h (room temperature), and then TMAOH was removed by one-time washing with deionized water. The resulted paste was dispersed into 1500 ml water and was delaminated by 10 min of handshaking, after which the dispersion was centrifuged at 3500 rpm for 1 h. The collected upper suspension was TM-$Ti_3C_2T_x$.

2.4. The fabrication of LH-$Ti_3C_2T_x$

1 g Ti_3AlC_2 powder was immersed into the mixture of 2 g LiF and 23 ml 9 M HCl, and was stirred in an oil bath at 60 °C for 48 h. Then the as-reacted product was repeatedly rinsed by water until the pH was over 6, and was dried by freeze drying to obtained multilayer $Ti_3C_2T_x$ (m-LH-$Ti_3C_2T_x$). The m-LH-$Ti_3C_2T_x$ was dispersed into 300 ml water and was sonicated for 1 h under flowing Ar, which followed by 1 h of centrifugation at 3500 rpm. Finally, the upper suspension was collected, which was named LH-$Ti_3C_2T_x$.

2.5. The annealing treat of $Ti_3C_2T_x$ conductive films

The concentration of $Ti_3C_2T_x$ suspension was measured by a UV–VIS spectrophotometer. And then a certain amount $Ti_3C_2T_x$ suspension was vacuum filtered and dried to obtain a $Ti_3C_2T_x$ conductive film with certain thickness. The film was transferred to glass slide and the filter membrane was dissolved by acetone. After that the conductive film with glass substrate was annealed by a tube furnace under Ar with a heating rate of 3 °C/min and was kept at 300 °C for 2 h, the as-produced was annealed $Ti_3C_2T_x$ conductive film.

2.6. The measurement of the resistance of $Ti_3C_2T_x$ films

Four silver electrodes were dotted on the $Ti_3C_2T_x$ films with the same thickness, the distance between each two silver electrodes was 1 cm, and the four electrodes were respectively four vertices of a square. Then, a digital multimeter was used to test the resistance of two adjacent silver electrodes separately and calculated the average value.

2.7. Characterization

The morphologies of the samples were observed by a field emission scanning electron microscope (SU8220, Hitachi, Japan) and a field emission transmission electron microscope (JEM-2100F, Hitachi, Japan). The phase composition was analyzed by a high-resolution multifunction X-ray diffractometer (D8 Discover Davinci, German) and the molecular structure was characterized by a Raman spectra (DXR spectrometer), an X-ray photoelectron spectroscopy (ESCAlab250, Thermo Fisher Scientific, Ameraic) and a ultraviolet visible light spectrophotometer (PerkinElmer Lambda 950 spectrometer). The electrical resistivity of the samples was measured by a four point probe and a digital multimeter. The bending test was conducted by a high-precision electronic universal testing machine (CMT6103, MTS Systems, China) and an electrochemical workstation (PARSTAT 2273, Princeton Applied Research).

3. Results and discussion

Fig. 1a schematically illustrates the fabrication progress of $Ti_3C_2T_x$ by the typical aqueous etching method, in which the Al atomic layer is selectively etched out from the original material Ti_3AlC_2 by reacting with acidic etchants (HF, LiF/HCl) or alkaline etchant (TMAOH) separately to obtain three kinds multilayer $Ti_3C_2T_x$. The HF-treated multilayer was further intercalated by dimethylsulfoxide (DMSO) and delaminated by sonication to obtain single or few layer $Ti_3C_2T_x$, while the multilayer samples etched by LiF/HCl as well as TMAOH were exfoliated by means of sonication or handshaking respectively. For the sake of brevity, the three final products were named as HF-$Ti_3C_2T_x$, LH-$Ti_3C_2T_x$ and TM-$Ti_3C_2T_x$ respectively according to the diverse etchants. The morphologies of multilayer $Ti_3C_2T_x$ samples are shown in Fig. 1b–d (Fig. S1), from which we can observe that the multilayer HF-$Ti_3C_2T_x$ and LH-$Ti_3C_2T_x$ are accordion-like bulks with myriad sheets orderly stacked, whereas the multilayer TM-$Ti_3C_2T_x$ is in the shape of two-dimensional thick paper, which exhibits a profound discrepancy with the former two. Through delamination, the HF-$Ti_3C_2T_x$ suspension presents
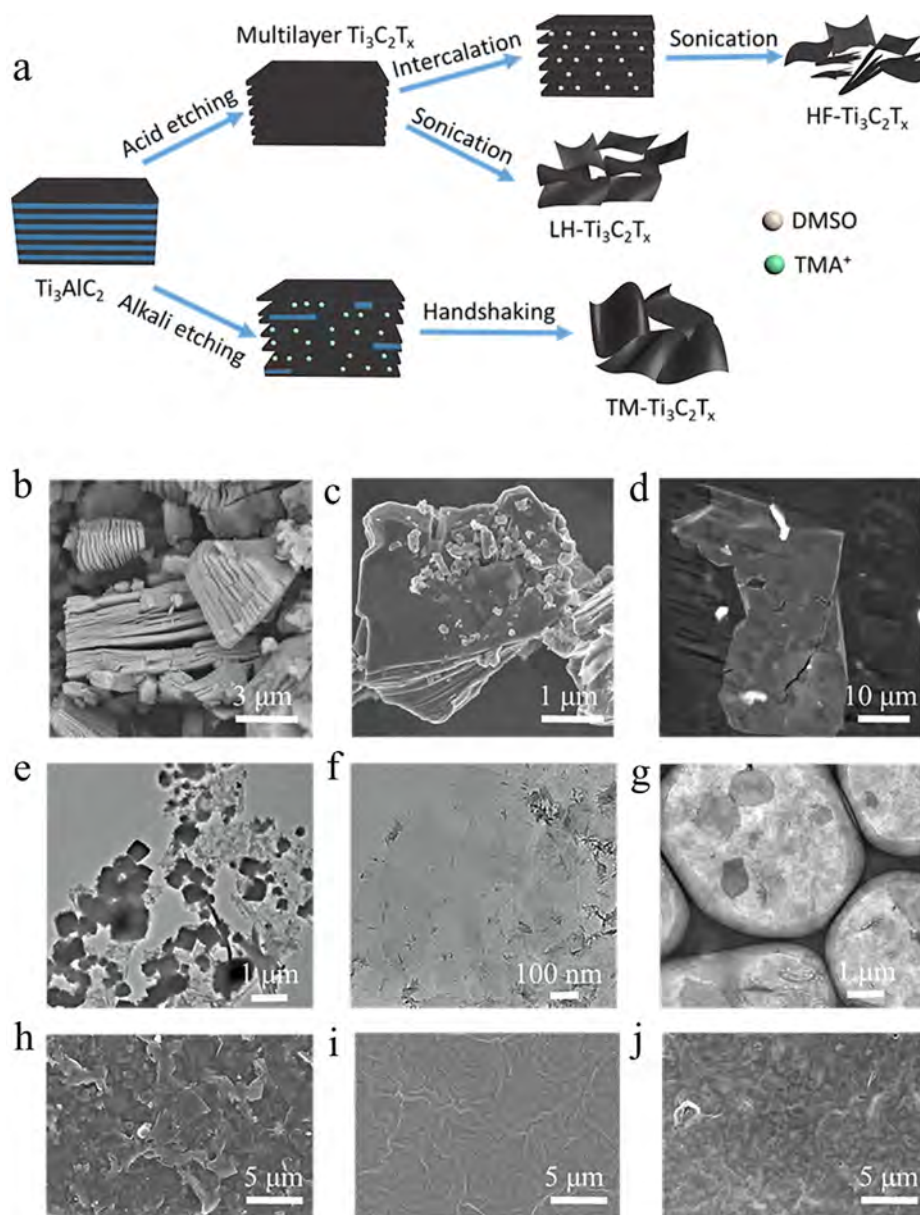
Fig. 1. (a) The schematic diagram of the preparation process of $Ti_3C_2T_x$. The top-view SEM images of multilayer (b) HF-$Ti_3C_2T_x$, (c) LH-$Ti_3C_2T_x$ and (d) TM-$Ti_3C_2T_x$. The TEM images of delaminated (e) HF-$Ti_3C_2T_x$, (f) LH-$Ti_3C_2T_x$ and (g) TM-$Ti_3C_2T_x$. The top-view SEM images of (h) HF-$Ti_3C_2T_x$, (i) LH-$Ti_3C_2T_x$ and (j) TM-$Ti_3C_2T_x$ conductive films.

a chaotic appearance, mainly consisting of small particles and sheets with varying size (Fig. 1e). The corresponding conductive film obtained by vacuum filtration is formed by randomly interlaced particles and sheets, and the surface looks rough (Fig. 1h). LH-$Ti_3C_2T_x$ and TM-$Ti_3C_2T_x$ are similar in morphology and are both composed of single or few flakes, except that the lateral size of flakes are 200–300 nm and several microns respectively (Fig. 1f–g). The flakes staked in order and tightly after filtration to form the corresponding films, whose surface are much smoother, although with some wrinkles (Fig. 1i–j). The great difference in the morphologies of the as prepared $Ti_3C_2T_x$ is closely involved with the ion composition and different function of the etchants. Although the highly corrosive HF is easily to break the Ti−Al bond, it will inevitably destroy the structure of $Ti_3C_2T_x$ itself at the same time, resulting in the multilayer bulks being pulverized to form small particles and flakes in the subsequent ultrasonic process. In contrast, the etching effect of LiF/HCl and TMAOH are much milder, and Li^+ and TMA^+ ions are intercalated into the adjacent sheets during the etching process to enlarge the interlayer spacing and facilitate

subsequent exfoliation, avoiding the use of additional intercalating agent and violent mechanical oscillation. As a result, the multilayer LH-$Ti_3C_2T_x$ and TM-$Ti_3C_2T_x$ are easier to be exfoliated and the morphologies are more uniform. Considering that the ionic radius of TMA^+ ion is larger than that of Li^+, the intercalation effect of TMA^+ on the multilayer $Ti_3C_2T_x$ is better, so that the multilayer sample is in the form of thick papers and can be completely exfoliated within only 10 min by handshaking, which greatly prevents the single- or few-layer $Ti_3C_2T_x$ flakes from forming fragments. Therefore, TM-$Ti_3C_2T_x$ exhibited the largest lateral size.

Fig. 2a shows the X-ray diffraction spectra (XRD) of Ti_3AlC_2 and the multilayer HF-$Ti_3C_2T_x$, LH-$Ti_3C_2T_x$ and TM-$Ti_3C_2T_x$. It was obviously that the characteristic peak of at 39° belonging to Ti_3AlC_2 disappeared in the multilayer HF-$Ti_3C_2T_x$ and LH-$Ti_3C_2T_x$, but was still existed in TM-$Ti_3C_2T_x$, indicating that the former two were completely transferred to $Ti_3C_2T_x$ phase, while the latter one was partially etched. As seen in Fig. S2, When using LiF and HCl acid as etchants, we changed the etching time and etching temperature to prepare $Ti_3C_2T_x$, and found
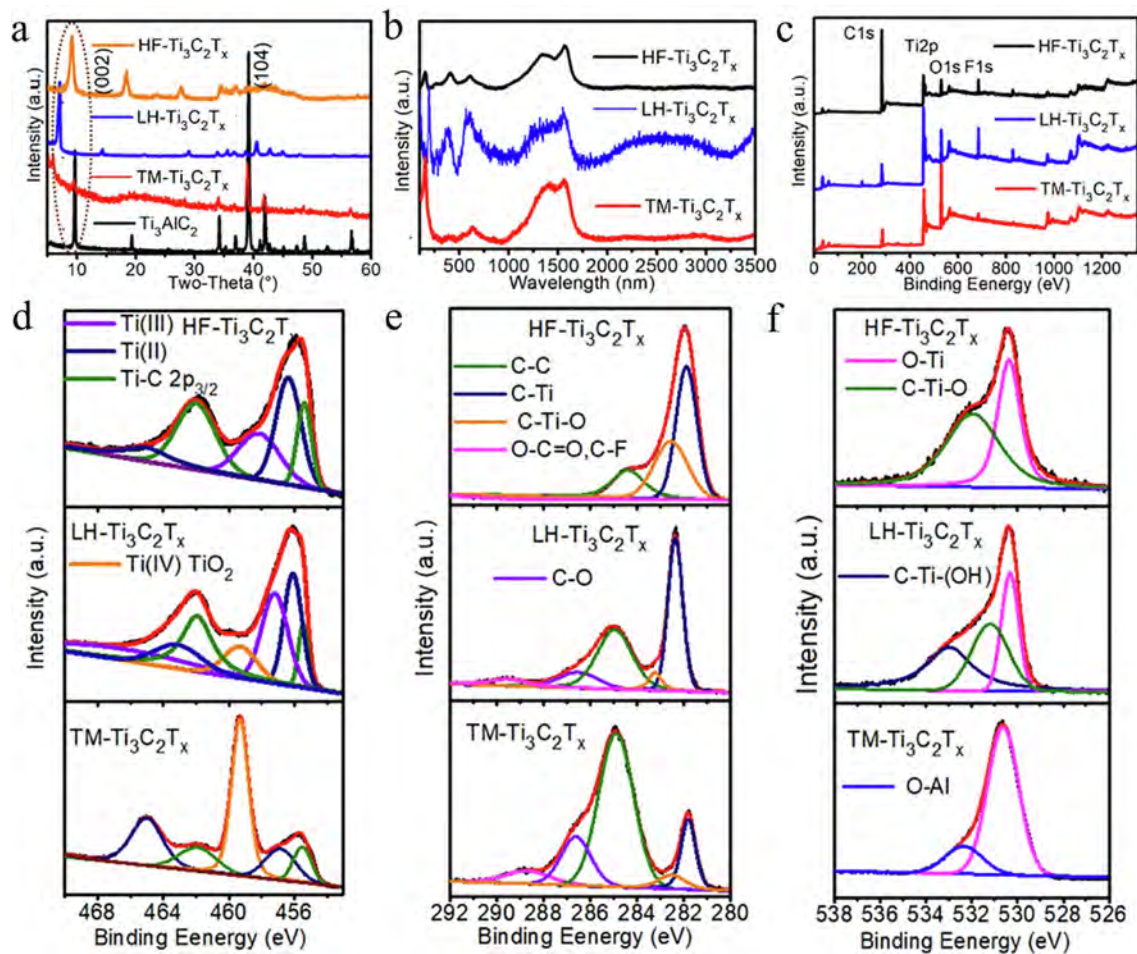
Fig. 2. The (a) XRD spectra of Ti_3AlC_2 and the multilayer HF-$Ti_3C_2T_x$, LH-$Ti_3C_2T_x$ and TM-$Ti_3C_2T_x$. The (b) Raman spectra, (c) XPS spectra, (d) XPS Ti2p spectra, (e) XPS C1s spectra, and (f) O1s spectra of HF-$Ti_3C_2T_x$, LH-$Ti_3C_2T_x$ and TM-$Ti_3C_2T_x$ conductive films.

that only the etching temperature was 60 °C and the etching time was 48 h can make Ti_3AlC_2 be completely etched. It was inconsistent with the reported literature that usually used 35 °C and 24 h as the etching conditions, which may be due to differences in the crystallinity of Ti_3AlC_2. TMAOH, as an etchant, was relatively mild, so it was not completely etched, but as seen in Fig. S2, the XRD pattern of TM-$Ti_3C_2T_x$ film showed that the characteristic peak of at 39° belonging to Ti_3AlC_2 completely disappeared, this result may be due to that the unetched Ti_3AlC_2 can be removed by centrifugation after delamination process, which will not affect subsequent research. The characteristic peaks of (0 0 2) lattice plane of the three multilayer samples were marked with dashed lines, and the 2θ values were 9.188°, 6.993°, 5.797° respectively. According to the Bragg formula, the corresponding interlayer spacing of HF-$Ti_3C_2T_x$, LH-$Ti_3C_2T_x$ and TM-$Ti_3C_2T_x$ were 9.6175 Å, 12.630 Å and 15.233 Å respectively, which further proved the notable intercalation effect of TMA^+ and Li^+ especial TMA^+. The Raman spectra of the delaminated $Ti_3C_2T_x$ conductive films are presented in Fig. 2b. The characteristic peak positions of LH-$Ti_3C_2T_x$ were consistent with those reported in the literature [34–35], and the peak at 602 cm^{-1} was related to the vibration of the carbon atoms of $Ti_3C_2T_x$. The spectra of HF-$Ti_3C_2T_x$ was almost the same as LH-$Ti_3C_2T_x$, except for the peak at 153 cm^{-1}, which may be due to the difference in surface terminations. The peaks at approximately 158, 392, 531 and 630 cm^{-1} of TM-$Ti_3C_2T_x$ were assigned to $E_{g(1)}$, $B1_{g(1)}$, A_{1g} & $B1_{g(2)}$, and $E_{g(3)}$ vibrational modes of anatase TiO_2, indicating the existence of TiO_2 in this sample [36–37]. It is worth mentioning that there was no characteristic peaks of Ti_3AlC_2 in the TM-$Ti_3C_2T_x$, which further confirmed the removing of un-etched MAX phase during delamination process. In

addition, there was a phenomenon that three samples all had characteristic peaks at around 1340 and 1580 cm^{-1}, corresponding to the D band and the G band of graphite carbon, respectively [15], wherein the relative intensity of the peak in HF-$Ti_3C_2T_x$ was larger, implying that the amorphous graphite content was higher. This can be explained by that the highly corrosive etchants dissolved a portion of Ti during the etching process, and HF exhibited the strongest corrosivity.

To further investigate the chemical components of the $Ti_3C_2T_x$ prepared by different etchants, the X-ray photoelectron spectra are demonstrated in Fig. 2c–f. The XPS spectra of HF-$Ti_3C_2T_x$, LH-$Ti_3C_2T_x$ and TM-$Ti_3C_2T_x$ films presented great differences in both the position and intensity of peaks. The atomic ratio of each sample was listed in Table 1. The content of C atom of HF-$Ti_3C_2T_x$ was high, which conformed to the results obtained by Raman spectra. In LH-$Ti_3C_2T_x$, the peak of Cl atom emerged, which may be caused by the fact that the etchant HCl was not completely removed, and similar results were found in XRD analysis. The contents of O atom and N atom were relatively high in TM-$Ti_3C_2T_x$, and it can be explained by the previous report that the exposed Ti atoms were attached by $Al(OH)_4^-$ as surface

Table 1
The atomic ratios of HF-$Ti_3C_2T_x$, LH-$Ti_3C_2T_x$ and TM-$Ti_3C_2T_x$.

Atomic%	C1s	O1s	Ti2p	F1s	Cl2p	N1s
HF-$Ti_3C_2T_x$	79.73	7.25	8.16	4.33	/	0.52
LH-$Ti_3C_2T_x$	40.00	19.41	27.83	8.99	2.43	1.33
TM-$Ti_3C_2T_x$	34.16	38.64	22.09	3.00	/	2.11

terminations, which was formed by the process of etching away Al atoms by OH^- in TMAOH and the TMA^+ intercalating into the adjacent layers during the etching progress [32].

From the XPS Ti2p region (Fig. 2d), the binding energies of approximately 455, 456, 458 and 569 eV were assigned to $Ti2p_{3/2}$ for Ti-C bond, Ti (II), Ti (III) and Ti (IV)-O bond respectively, and the binding energies above 460 eV presented the corresponding peaks of $Ti2p_{1/2}$ electron orbit [38–39]. Obviously, Ti (IV)-O bond was much stronger in TM-$Ti_3C_2T_x$ than the other two samples and was absent in HF-$Ti_3C_2T_x$, which well identified the results of the Raman analysis. The peaks corresponding to Ti (III) in samples HF-$Ti_3C_2T_x$ and LH-$Ti_3C_2T_x$ were located at 458.2 and 457.2 eV, respectively. The difference in the position of Ti (III) between the two samples was mainly contributed to the difference in the surface terminations connected to Ti (III). The F/Ti atom ratio of HF-$Ti_3C_2T_x$ in Table 1 was much higher than that of LH-$Ti_3C_2T_x$, which indicated that HF-$Ti_3C_2T_x$ contained more -F terminations. This result was contributed to that the F content of the HF used is much higher than that of LiF. The C1s region (Fig. 2e) provides the information that the C–Ti–O bond (about 283 eV) is strong in HF-$Ti_3C_2T_x$, accounting for the high content of O terminations, while the peak corresponding to C–Ti–O and C–Ti–(OH) were both existed in LH-$Ti_3C_2T_x$, illustrating that −O/−OH terminations were dominant in this sample. TM-$Ti_3C_2T_x$ contained more C–C and O–C=O bonds, which may be from the ramifications of residual organic base etchant. Besides, compared with TM-$Ti_3C_2T_x$, a shift to higher energies for the C–Ti and C–Ti–O bonds in HF-$Ti_3C_2T_x$ and LH-$Ti_3C_2T_x$ was observed (the C-Ti peaks of HF-$Ti_3C_2T_x$, LH-$Ti_3C_2T_x$ and TM-$Ti_3C_2T_x$ were at 282.25, 282.3 and 281.85 eV respectively, and C–Ti–O peaks were at 282.85, 283.2 and 282.55 eV respectively). This result can be explained by the fact that in HF-$Ti_3C_2T_x$ and LH-$Ti_3C_2T_x$, −OH and −F may withdraw valence electrons from Ti atoms and subsequently from C atoms when substituted gallery Al atoms, but it was not occurred in TM-$Ti_3C_2T_x$ owing to the additional electron injection from Al atoms through Al−O bonding. The formation of Al−O bond was confirmed in O1s spectra (Fig. 2f), further proving that $Al(OH)_4^-$ bonded to TM-$Ti_3C_2T_x$ as surface terminations by bonding its O atoms to Ti atoms [32,40]. In conclusion, the surface terminations in HF-$Ti_3C_2T_x$ mainly consists of −F and −O, and −OH and −O are dominant terminations in LH-$Ti_3C_2T_x$, while TM-$Ti_3C_2T_x$ is mainly attached by $Al(OH)_4^-$, which is in accordance with the references [32].

To investigate the stability of the $Ti_3C_2T_x$ samples fabricated by varying etchants, we analyzed the change in morphologies and compositions of the fresh samples and the samples aged in atmosphere at room temperature for 30 days (named as 30-day-samples). Fig. 3a–c show the transmission electron microscope (TEM) images of 30-day-HF-$Ti_3C_2T_x$, 30-day-LH-$Ti_3C_2T_x$ and 30-day-TM-$Ti_3C_2T_x$ suspensions. Noteworthy changes were observed on the morphologies of the samples, as shown in Fig. 1e–g. Both $Ti_3C_2T_x$ flakes and particles decomposed after aging. In detail, the particles in fresh HF-$Ti_3C_2T_x$ were degraded from a few microns to about 100 nm, and the sheets with the size of 200–300 nm in fresh LH-$Ti_3C_2T_x$ or several microns in fresh TM-$Ti_3C_2T_x$ were degraded into dozens of nanometers in size. The variations in chemical components of the 30-day-samples were characterized by selected area electron diffraction (SAED). The SAED patterns of 30-day-HF-$Ti_3C_2T_x$ and 30-day-LH-$Ti_3C_2T_x$ were the same, corresponding to the tetragonal titanium oxide, indicating that the sample had undergone a oxidation reaction, while the pattern of 30-day-TM-$Ti_3C_2T_x$ corresponded to the simple cubic aluminum hydroxide, which may be derived from $Al(OH)_4^-$ surface terminations. According to the Beer-Lambert Law (Formula (1)) [41], the intensity of Ultraviolet and visible (UV–VIS) absorption is proportional to the concentration of suspension.

$$A = lg(1/T) = Kbc \tag{1}$$

A—absorbance, T—transmittance, K—molar absorptivity, c—concentration of the test sample, b—thickness of the absorbing layer.

So that a UV–VIS absorption spectrum was employed to track the

change in the concentration of $Ti_3C_2T_x$ suspensions to assess the degree of degradation during 30 days (Fig. 3d–e). Notably, there were great differences in the positions and intensities of minimum absorption wavelength (λ_{min}) of the three fresh $Ti_3C_2T_x$ samples. The different positions of λ_{min} may be resulted from the difference in surface terminations, and for HF-$Ti_3C_2T_x$, LH-$Ti_3C_2T_x$ and TM-$Ti_3C_2T_x$, the λ_{min} were located at approximately 650, 550, and 600 nm, respectively. The diversity in intensities can be attributed to the inconsistence in the initial concentrations of the fresh samples because that the degree of delamination varied depending on the etching conditions used. After 30 days, the λ_{min} of HF-$Ti_3C_2T_x$, LH-$Ti_3C_2T_x$ and TM-$Ti_3C_2T_x$ showed a significant red shift, and the intensities were significantly reduced, respectively attenuating to 6.41%, 0.16% and 1.4% of the corresponding fresh samples. Fig. S4a–c and Fig. 3e record the UV–VIS spectrum and λ_{min} of each $Ti_3C_2T_x$ suspension aged in atmosphere at room temperature for 30 consecutive days. For HF-$Ti_3C_2T_x$ suspension, the intensity of λ_{min} exhibited a rapid decline in the first 6 days, corresponding to the sedimentation of the unstable particles and flakes, after which the intensity slowly decreased and the color of the suspension gradually changed from dark green to milky white, similar to the color of TiO_2 sol (Fig. S5c). Analogously, the intensity of λmin of LH-$Ti_3C_2T_x$ decreased suddenly after 3 days due to the severe flocculation of the $Ti_3C_2T_x$ flakes (Fig. S5d). By contrast, the concentration of TM-$Ti_3C_2T_x$ suspension went through a relatively steady variation and the color of the suspension gradually became lighter and there was no sedimentation at the bottom of the container (Fig. S5e), indicating that TM-$Ti_3C_2T_x$ had a good dispersibility and a uniform metamorphic process.

Fig. 3f demonstrates the XPS Ti2p spectrum of the HF-$Ti_3C_2T_x$, LH-$Ti_3C_2T_x$ and TM-$Ti_3C_2T_x$ conductive films stored in air at room temperature for 30 days (the corresponding XPS C1s and O1s spectrums are presented in Fig. S6). The peak of Ti (IV)−O bond appeared in HF-$Ti_3C_2T_x$ and enhanced in LH-$Ti_3C_2T_x$, but remained almost unchanged in TM-$Ti_3C_2T_x$ film, implying that HF-$Ti_3C_2T_x$, LH-$Ti_3C_2T_x$ underwent relatively significant oxidation while TM-$Ti_3C_2T_x$ kept stable. However, Raman spectrum (Fig. S7) and XRD pattern (Fig. S8) of $Ti_3C_2T_x$ films showed little variation before and after 30 days aging, illustrating that there were traces of the oxidative products in the films and may be mainly concentrated on the surface of the films. It also indicated that the antioxidation ability of the dried conductive film was much better than that of the corresponding aqueous dispersion, revealing that dissolved oxygen in water was the main factor to accelerate the oxidation process, which was in accordance with the previous report.

$$k = Ae - Ea/RT \tag{2}$$

k—rate constant, R—molar gas constant, T—thermodynamic temperature, Ea—apparent activation energy, A—pre-factor (also called the frequency factor).

According to the Arrhenius formula (Formula (2)), [42] the reaction rate is inversely related to the reaction temperature. Therefore, the fresh $Ti_3C_2T_x$ suspensions were stored at temperature of 4 °C in order to slow down the degradation process, and the UV–Vis spectrums were also applied to quantify the degree of degradation during consecutive 30 days. As shown in Fig. S4d–f and Fig. S5a, HF-$Ti_3C_2T_x$ and LH-$Ti_3C_2T_x$ suspensions at 4 °C exhibited different levels of sedimentation in the first 6 days and the first 10 days respectively, and the positions of λ_{min} also demonstrated an obvious red shift, similar to the phenomenon under room temperature. On the contrary, the sedimentation didn't appear and the red shift was not obvious in TM-$Ti_3C_2T_x$ suspension. The λ_{min} of HF-$Ti_3C_2T_x$, LH-$Ti_3C_2T_x$ and TM-$Ti_3C_2T_x$ decreased in intensity to 24.07%, 4.16% and 59.96% respectively after 30 days at low temperature, which were higher than those stored at room temperature, confirming that the preservation at low temperature was very effective (Fig. S5b–e). In conclusion, an anhydrous and low temperature environment is beneficial to slow down the rate of degradation of $Ti_3C_2T_x$, whcih was consistent with previous literature reports [36]. And among the three $Ti_3C_2T_x$ samples, TM-$Ti_3C_2T_x$ has the best anti-degradation
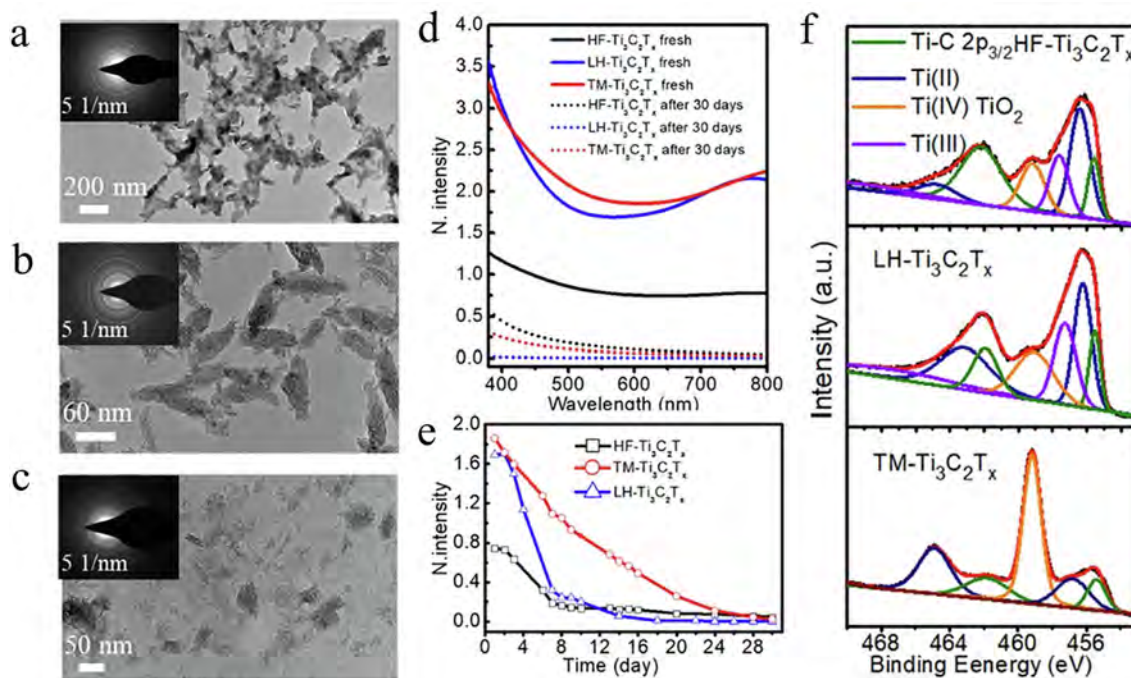
Fig. 3. The TEM images of (a) HF-Ti$_3$C$_2$T$_x$, (b) LH-Ti$_3$C$_2$T$_x$ and (c) TM-Ti$_3$C$_2$T$_x$ suspensions which are aged in atmosphere at room temperature (RT) for 30 days. The insets are the corresponding selected electron diffraction patterns of the samples. (d) The ultraviolet-visible spectrum of Ti$_3$C$_2$T$_x$ suspensions before and after 30 days. (e) The change in intensity of UV absorbance bands of Ti$_3$C$_2$T$_x$ suspensions during 30 days. (f) The XPS Ti2p spectra of Ti$_3$C$_2$T$_x$ films after 30 days.

ability, which may be benefited by the Al(OH)$_4$- terminations and the protection from TMA$^+$.

The electronic properties and mechanical properties of the three typical Ti$_3$C$_2$T$_x$ samples above were also measured in Fig. 4. The resistance of Ti$_3$C$_2$T$_x$ conductive films with a consistent thickness was record continuously during 60 days by a digital multimeter shown in Fig. 4a. As seen in Fig. S9, the thicknesses of three Ti$_3$C$_2$T$_x$ conductive films were 400 nm. The initial resistance per centimeter of HF-Ti$_3$C$_2$T$_x$, LH-Ti$_3$C$_2$T$_x$ and TM-Ti$_3$C$_2$T$_x$ films were 5.69 kΩ, 27.48 Ω and 20.1 Ω, respectively, which were in great difference with each other. It is obviously that the conductivity of LH-Ti$_3$C$_2$T$_x$ and TM-Ti$_3$C$_2$T$_x$ was more than 200 times higher than HF-Ti$_3$C$_2$T$_x$. This phenomenon can be mainly explained by the fact that the HF-Ti$_3$C$_2$T$_x$ film mainly consisted of randomly stacked small particles and sheets had a larger contact resistance, while the LH-Ti$_3$C$_2$T$_x$ and TM-Ti$_3$C$_2$T$_x$ film comprised of orderly stacked sheets had smaller contact resistances. Furthermore, TM-Ti$_3$C$_2$T$_x$ had a larger lateral size, which is beneficial to decrease the contact resistance. Therefore, TM-Ti$_3$C$_2$T$_x$ film exhibited the lowest Initial resistance. After aging in atmosphere for 60 days, the resistance of HF-Ti$_3$C$_2$T$_x$, LH-Ti$_3$C$_2$T$_x$ and TM-Ti$_3$C$_2$T$_x$ films increased by 10.38, 2.64 and 1.67 times respectively, which were well in accordance with the stability of each sample.

The Ti$_3$C$_2$T$_x$ films with varying thickness were fabricated and annealed at 300 °C under the protection of Ar for 2 h to investigate the influence of the annealing treatment and thickness on the conductivity of Ti$_3$C$_2$T$_x$ films. As shown in Fig. 4b-d, the sheet resistances of HF-Ti$_3$C$_2$T$_x$, LH-Ti$_3$C$_2$T$_x$ and TM-Ti$_3$C$_2$T$_x$ films with varying thickness all decreased in different degree after annealing, and the variation in resistance was in proportion to the thickness of the film (the HF-Ti$_3$C$_2$T$_x$ films with the thickness less than 200 nm were not conductive). These results can be resulted from the partial removal of surface terminations (−OH, −O, −F and Al(OH)$_4^-$) and intercalations (H$_2$O, DMSO and TMA$^+$) after annealing, and the thicker the film, the more surface terminations and intercalations were removed, leading to greater change in resistance. In addition, the TM-Ti$_3$C$_2$T$_x$ films performed the largest reduction in sheet resistance after annealing (Fig. 4e), which was nearly 3 times decrease when the thickness of the film was 400 nm,

while the resistance of the HF-Ti$_3$C$_2$T$_x$ films reduced the least. It can be explained by that the TMA$^+$ contained in TM-Ti$_3$C$_2$T$_x$ may have a greater influence on electrical resistance than other factors, and another reason was that the ratio of O terminations in HF-Ti$_3$C$_2$T$_x$ was higher, which were more stable than the F terminations according to previous reports, so that the effect of annealing was weak in this sample. In a word, in the case of uniform film thickness, the TM-Ti$_3$C$_2$T$_x$ film exhibited the lowest resistance and best anti-degradation ability, and the largest enhancement of conductivity after annealing. While the HF-Ti$_3$C$_2$T$_x$ film was the least prominent in all respects.

The cyclic bending tests of Ti$_3$C$_2$T$_x$ films are presented in Fig. 4f-h to evaluate the flexibility, which are processed by attaching the Ti$_3$C$_2$T$_x$ films to a PET film and connecting the electrodes at the both ends to track the current signal of the samples during the cyclic bending process. Obviously, the current intensity of the HF-Ti$_3$C$_2$T$_x$ film gradually attenuated during the cyclic bending process of 500 times with the bending angle of 30°. In case of the cyclic bending test conditions were consistent, the LH-Ti$_3$C$_2$T$_x$ film performed a rapid decrease in current and amplitude in the first 150 cycles, and then maintained very small current signals and amplitudes up to 500 cycles. And for the TM-Ti$_3$C$_2$T$_x$ film, the current signal was not stable throughout the bending test and the current-cycle curve was irregular with many points of discontinuity. The difference in the flexibility of Ti$_3$C$_2$T$_x$ samples can be traced back to the difference in the morphologies. The LH-Ti$_3$C$_2$T$_x$ and TM-Ti$_3$C$_2$T$_x$ films were composed of tightly stacked sheets, in which the adjacent sheets were interacted with each other and could not realize effective slippage, so that large cracks generated easily during the bending process to destroy the conductive networks, while the small particles existed in the HF-Ti$_3$C$_2$T$_x$ film restrained the close stacking of the sheets and played a certain role of lubrication to promote the sliding of Ti$_3$C$_2$T$_x$ sheets and protect the conductive pathways. It is worth noting that even though Ti$_3$C$_2$T$_x$ is a two-dimensional material, its flexibility may be inferior to the carbon based low dimensional materials due to its ceramic nature.
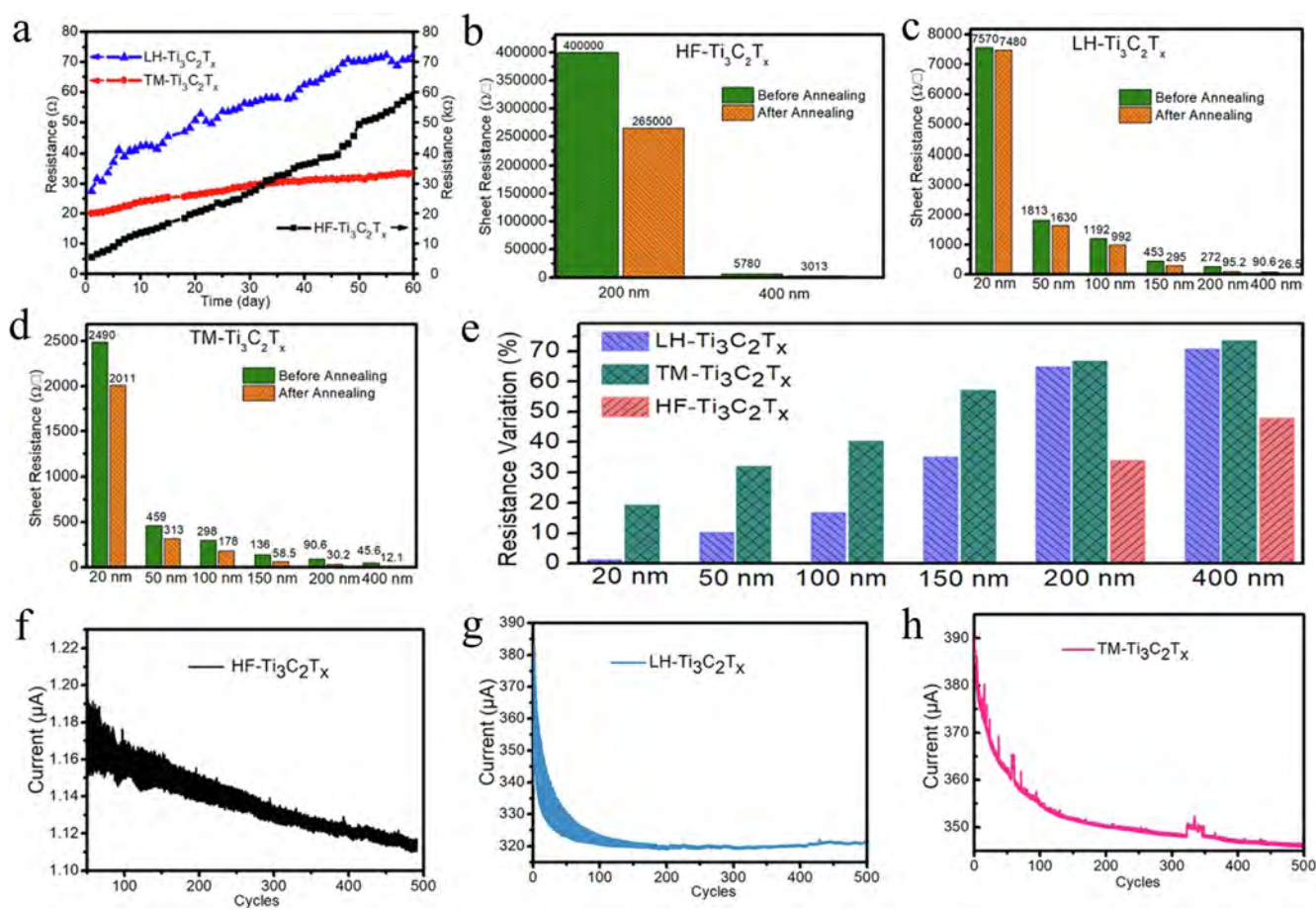
Fig. 4. (a) The resistance per centimeter of $Ti_3C_2T_x$ conductive films (the thickness is 400 nm) during 60 days. The sheet resistance of (b) HF-$Ti_3C_2T_x$, (c) LH-$Ti_3C_2T_x$ and (d) TM-$Ti_3C_2T_x$ films before and after annealing. (e) The resistance variation of $Ti_3C_2T_x$ conductive films with different thickness before and after annealing. The bending cycle test of (f) HF-$Ti_3C_2T_x$, (g) LH-$Ti_3C_2T_x$ and (h) TM-$Ti_3C_2T_x$ films with the bending angle of 30°.

4. Conclusion

In this work, the differences in morphology and surface terminations of the $Ti_3C_2T_x$ samples fabricated by three typical etching agents were systematically investigated. And the enhancement of stability, conductivity and flexibility were also discovered. It is found that HF-$Ti_3C_2T_x$ consisted of both particles and sheets, with −O and −F as leading terminations, while LH-$Ti_3C_2T_x$ was mainly composed of small-sized sheets, containing a large number −O/−OH terminations, and TM-$Ti_3C_2T_x$ was also composed of sheets with a larger size, containing Al(OH)$_4^-$ terminations. The priorities in stability and conductivity of the three were TM-$Ti_3C_2T_x$, LH-$Ti_3C_2T_x$ and HF-$Ti_3C_2T_x$, respectively, and the flexibility was reversed, which revealed that larger lamellar size and compact microstructure were favorable for enhancing conductivity and stability, while the interlamellar interaction is the dominating factors to the flexibility. This work systematically summarized the influence of etching conditions on the properties of $Ti_3C_2T_x$, effectively facilitating the tailoring of $Ti_3C_2T_x$ for specific fields according to different requirements.

CRediT authorship contribution statement

Yina Yang: Conceptualization, Methodology, Investigation, Visualization, Writing - original draft, Writing - review & editing, Funding acquisition. **Zherui Cao:** Resources, Methodology. **Liangjing Shi:** Investigation. **Ranran Wang:** Supervision, Funding acquisition. **Jing Sun:** Supervision.

Declaration of Competing Interest

The authors declare that they have no known competing financial interests or personal relationships that could have appeared to influence the work reported in this paper.

Acknowledgements

Appendix A. Supplementary material

Supplementary data to this article can be found online at https://doi.org/10.1016/j.apsusc.2020.147475.

References

[1] M. Naguib, M. Kurtoglu, V. Presser, J. Lu, J. Niu, M. Heon, L. Hultman, Y. Gogotsi, M.W. Barsoum, Two-dimensional nanocrystals produced by exfoliation of Ti3AlC2, Adv. Mater. 23 (2011) 4248–4253.
[2] M. Naguib, O. Mashtalir, J. Carle, V. Presser, J. Lu, L. Hultman, Y. Gogotsi, M.W. Barsoum, Two-dimensional transition metal carbides, ACS Nano 6 (2) (2012) 1322–1331.
[3] M. Naguib, V.N. Mochalin, M.W. Barsoum, Y. Gogotsi, 25th anniversary article: MXenes: a new family of two-dimensional materials, Adv. Mater. 26 (2014) 992–1005.

[4] Babak Anasori, Yu Xie, Majid Beidaghi, Jun Lu, Brian C. Hosler, Lars Hultman, Paul R.C. Kent, Yury Gogotsi, Michel W. Barsoum, Two-dimensional, ordered, double transition metals carbides (MXenes), ACS Nano 9 (2015) 9507–9516.

[5] B. Anasori, M.R. Lukatskaya, Y. Gogotsi, 2D metal carbides and nitrides (MXenes) for energy storage, Nat. Rev. Mater. 2 (2) (2017) 16098.

[6] M. Khazaei, A. Ranjbar, M. Arai, T. Sasaki, S. Yunoki, Electronic properties and applications of MXenes: a theoretical review, J. Mater. Chem. C. 5 (2017) 2488–2503.

[7] I.R. Shein, A.L. Ivanovskii, Graphene-like nanocarbides and nanonitrides of d metals (MXenes): synthesis, properties and simulation. Micro & Nano Lett. 8 (2013) 59–62.

[8] A.L. Ivanovskii, A.N. Enyashin, Graphene-like transition-metal nanocarbides and nanonitrides, Russ. Chem. Rev. 82 (8) (2013) 735–746.

[9] J.-C. Lei, X.u. Zhang, Z. Zhou, Recent advances in MXene: Preparation, properties, and applications, Front. Phys. 10 (3) (2015) 276–286.

[10] T. Shang, Z. Lin, C. Qi, X. Liu, P. Li, Y. Tao, Z. Wu, D. Li, P. Simon, Q.-H. Yang, 3D Macroscopic Architectures from Self-Assembled MXene Hydrogels, Adv. Funct. Mater. 29 (33) (2019) 1903960.

[11] M.-Q. Zhao, X. Xie, C.E. Ren, T. Makaryan, B. Anasori, G. Wang, Y. Gogotsi, Hollow MXene Spheres and 3D Macroporous MXene Frameworks for Na-Ion Storage, Adv. Mater. 29 (37) (2017) 1702410.

[12] X. Wu, Z. Wang, M. Yu, L. Xiu, J. Qiu, Stabilizing the MXenes by carbon nanoplating for developing hierarchical nanohybrids with efficient lithium storage and hydrogen evolution capability, Adv. Mater. 29 (24) (2017) 1607017.

[13] F. Shahzad, M. Alhabeb, C.B. Hatter, B. Anasori, S. Man Hong, C.M. Koo, Y. Gogotsi, Electromagnetic interference shielding with 2D transition metal carbides (MXenes), Science 353 (6304) (2016) 1137–1140.

[14] J.i. Liu, H.-B. Zhang, R. Sun, Y. Liu, Z. Liu, A. Zhou, Z.-Z. Yu, Hydrophobic, flexible, and lightweight MXene foams for high-performance electromagnetic-interference shielding, Adv. Mater. 29 (38) (2017) 1702367.

[15] M. Han, X. Yin, H. Wu, Z. Hou, C. Song, X. Li, L. Zhang, L. Cheng, Ti3C2 MXenes with Modified Surface for High-Performance Electromagnetic Absorption and Shielding in the X-Band, ACS Appl. Mater. Interfaces. 8 (2016) 21011–21019.

[16] K. Li, T. Jiao, R. Xing, G. Zou, Q. Zhao, J. Zhou, L. Zhang, Q. Peng, Fabrication of hierarchical MXene-based AuNPs-containing core–shell nanocomposites for high efficient catalysts, Green Energy Environ. 3 (2018) 147–155.

[17] K. Li, T. Jiao, R. Xing, G. Zou, J. Zhou, L. Zhang, Q. Peng, Fabrication of tunable hierarchical MXene@AuNPs nanocomposites constructed by self-reduction reactions with enhanced catalytic performances, Sci. China Mater. 61 (2018) 728–736.

[18] J.-H. Pu, X. Zhao, X.-J. Zha, L. Bai, K. Ke, R.-Y. Bao, Z.-Y. Liu, M.-B. Yang, W. Yang, Multilayer structured AgNW/WPU-MXene fiber strain sensors with ultrahigh sensitivity and a wide operating range for wearable monitoring and healthcare, J. Mater. Chem. A. 7 (2019) 15913–15923.

[19] Y. Yang, L. Shi, Z. Cao, R. Wang, J. Sun, Strain Sensors with a High Sensitivity and a Wide Sensing Range Based on a Ti 3 C 2 T x (MXene) Nanoparticle–Nanosheet Hybrid Network, Adv. Funct. Mater. 29 (14) (2019) 1807882.

[20] Y. Yang, Z. Cao, P. He, L. Shi, G. Ding, R. Wang, J. Sun, Ti$_3$C$_2$T$_x$ MXene-graphene composite films for wearable strain sensors featured with high sensitivity and large range of linear response, Nano Energy 66 (2019) 104134.

[21] X. Yu, J. Cheng, Z. Liu, Q. Li, W. Li, X. Yang, B. Xiao, The band gap modulation of monolayer Ti$_2$CO$_2$ by strain, RSC Adv. 5 (2015) 30438–30444.

[22] D. Magne, V. Mauchamp, S. Celerier, P. Chartier, T. Cabioc'h, Site-projected electronic structure of two-dimensional Ti$_3$C$_2$ MXene: the role of the surface functionalization groups, Phys. Chem. Chem. Phys. 18 (2016) 30946–30953.

[23] A.N. Enyashin, A.L. Ivanovskii, Atomic structure, comparative stability and electronic properties of hydroxylated Ti$_2$C and Ti$_3$C$_2$ nanotubes, Comput. Theor. Chem. 989 (2012) 27–32.

[24] Y. Jiang, T. Sun, X. Xie, W. Jiang, J. Li, B. Tian, C. Su, Oxygen-Functionalized Ultrathin Ti$_3$C$_2$T$_x$ MXene for Enhanced Electrocatalytic Hydrogen Evolution, Chem. Sus. Chem. 12 (2019) 1368–1373.

[25] T. Schultz, N.C. Frey, K. Hantanasirisakul, S. Park, S.J. May, V.B. Shenoy, Y. Gogotsi, N. Koch, Surface termination dependent work function and electronic properties of Ti3C2Tx MXene, Chem. Mater. 31 (2019) 6590–6597.

[26] S. Lai, J. Jeon, S.K. Jang, J. Xu, Y.J. Choi, J.-H. Park, E. Hwang, S. Lee, Surface group modification and carrier transport properties of layered transition metal carbides (Ti 2 CT x , T: –OH, –F and –O), Nanoscale 7 (46) (2015) 19390–19396.

[27] Y. Dong, S.S.K. Mallineni, K. Maleski, H. Behlow, V.N. Mochalin, A.M. Rao, Y. Gogotsi, R. Podila, Metallic MXenes: A new family of materials for flexible tri-boelectric nanogenerators, Nano Energy. 44 (2018) 103–110.

[28] H. Lin, X. Wang, L. Yu, Y. Chen, J. Shi, Two-dimensional ultrathin MXene ceramic nanosheets for photothermal conversion, Nano Lett. 17 (2017) 384–391.

[29] W. Cao, W. Feng, Y. Jiang, C. Ma, Z. Zhou, M. Ma, Y. Chen, F. Chen, Two-dimensional MXene-reinforced robust surface superhydrophobicity with self-cleaning and photothermal-actuating binary effects, Mater. Horiz. 6 (2019) 1057–1065.

[30] L. Xiu, Z. Wang, M. Yu, X. Wu, J. Qiu, Aggregation-resistant 3D MXene-based architecture as efficient bifunctional electrocatalyst for overall water splitting, ACS Nano. 12 (2018) 8017–8028.

[31] H. Zhuo, Y. Hu, Z. Chen, X. Peng, L. Liu, Q. Luo, J. Yi, C. Liu, L. Zhong, A carbon aerogel with super mechanical and sensing performances for wearable piezo-resistive sensors, J. Mater. Chem. A. 7 (2019) 8092–8100.

[32] J. Xuan, Z. Wang, Y. Chen, D. Liang, L. Cheng, X. Yang, Z. Liu, R. Ma, T. Sasaki, F. Geng, Organic-base-driven intercalation and delamination for the production of functionalized titanium carbide nanosheets with superior photothermal therapeutic performance, Angew. Chem. Int. Ed. 55 (2016) 1–7.

[33] M. Ghidiu, M.R. Lukatskaya, M.Q. Zhao, Y. Gogotsi, M.W. Barsoum, Conductive two-dimensional titanium carbide 'clay' with high volumetric capacitance, Nature. 516 (2014) 78–81.

[34] M. Naguib, O. Mashtalir, M.R. Lukatskaya, B. Dyatkin, C. Zhang, V. Presser, Y. Gogotsi, M.W. Barsoum, One-step synthesis of nanocrystalline transition metal oxides on thin sheets of disordered graphitic carbon by oxidation of MXenes, Chem. Commun. 50 (2014) 7420–7423.

[35] L. Wang, H. Zhang, B. Wang, C. Shen, C. Zhang, Q. Hu, A. Zhou, B. Liu, Synthesis and electrochemical performance of Ti$_3$C$_2$T$_x$ with hydrothermal process, Electron. Mater. Lett. 12 (2016) 702–710.

[36] Y. Chae, S.J. Kim, S.Y. Cho, J. Choi, K. Maleski, B.J. Lee, H.T. Jung, Y. Gogotsi, Y. Lee, C.W. Ahn, An investigation into the factors governing the oxidation of two-dimensional Ti$_3$C$_2$ MXene, Nanoscale. 11 (2019) 8387–8393.

[37] X. Zhao, A. Vashisth, E. Prehn, W. Sun, S.A. Shah, T. Habib, Y. Chen, Z. Tan, J.L. Lutkenhaus, M. Radovic, M.J. Green, Antioxidants Unlock Shelf-Stable Ti$_3$C$_2$T$_x$ (MXene) Nanosheet Dispersions, Matter. 1 (2019) 513–526.

[38] J. Halim, K.M. Cook, M. Naguib, P. Eklund, Y. Gogotsi, J. Rosen, M.W. Barsoum, X-ray photoelectron spectroscopy of select multi-layered transition metal carbides (MXenes), Appl. Surf. Sci. 362 (2016) 406–417.

[39] A. Qian, J.Y. Seo, H. Shi, J.Y. Lee, C.H. Chung, Surface functional groups and electrochemical behavior in dimethyl sulfoxide-delaminated Ti3C2Tx MXene, Chem. Sus. Chem. 11 (2018) 3719–3723.

[40] J. Halim, M.R. Lukatskaya, K.M. Cook, J. Lu, C.R. Smith, L.A. Naslund, S.J. May, L. Hultman, Y. Gogotsi, P. Eklund, M.W. Barsoum, Transparent conductive two-dimensional titanium carbide epitaxial thin films, Chem. Mater. 26 (2014) 2374–2381.

[41] Earlene Atchison, H.E. Moore, Jr., C.E. Wood, Jr, The application of the beer-lambert law to optically anisotropic systems, Science 110(1949), 41-43.

[42] W. Tang, Y. Liu, H. Zhang, C. Wang, New approximate formula for Arrhenius temperature integral, Thermochim. Acta. 408 (2003) 39–43.